Check for updates

# Polypyrrole–methylene blue nanoparticles as a single multifunctional nanoplatform for near-infrared photo-induced therapy and photoacoustic imaging†

Thi Tuong Vy Phan,[ac] Subramaniyan Bharathiraja,[a] Van Tu Nguyen,[ac] Madhappan Santha Moorthy,[a] Panchanathan Manivasagan,[a] Kang Dae Lee[d] and Junghwan Oh ⓘ *[ab]

The combination of photothermal therapy (PTT) and photodynamic therapy (PDT) has recently gained much attention due to its selective and localized therapeutic effects by light irradiation. The reagents for phototherapy should have a large absorption coefficient in the near infrared region (NIR) (700 to 2500 nm) to maximize the depth of light penetration in tissues. In this study, we designed multifunctional nanoparticles that can provide strong NIR absorbing capability for the combined treatment of PTT and PDT. For the first time, FDA-approved photosensitizer methylene blue (MB) was conjugated with photothermal material polypyrrole (PPy) to form a novel NIR photo-absorber. The obtained PPy–MB NPs with an average size of 48.5 nm showed excellent biocompatibility, photothermal stability, and high NIR absorbance for the combined PTT and PDT. Under a NIR laser (*e.g.*, 808 nm laser) at 0.5 W cm$^{-2}$, the temperature of the aqueous solution containing 50 μg ml$^{-1}$ PPy–MB NPs reached up to 50 °C within a very short time and reactive oxygen species (ROS) were also generated. *In vitro* investigation confirmed the effectiveness of the PPy–MB NPs in killing the cancer cells under the NIR laser. Further, the phantom test of photoacoustic microscopy (PAM) used in conjunction with PPy–MB NPs showed a strong photoacoustic signal. Therefore, the novel PPy–MB NPs could be considered as promising single multifunctional nanoplatforms for further applications of photo-induced therapy and biomedical imaging.

## 1. Introduction

Combined therapy using multifunctional nanoparticles can be a highly promising strategy to enhance anticancer efficacy with minimum side effects.[1–3] Among several combined therapies employed, the combination of photothermal therapy (PTT) and photodynamic therapy (PDT) has recently attracted much attention due to its selective and localized therapeutic effects by light irradiation.[4] The contrast agents for phototherapy should have a large absorption coefficient in the near infrared region (NIR) (700–2500 nm) where the light has its maximum depth of

*[a]Marine-Integrated Bionics Research Center, Pukyong National University, Busan 48513, Republic of Korea. E-mail: jungoh@pknu.ac.kr; Fax: +82-51-629-5779; Tel: +82-51-629-5771*

*[b]Department of Biomedical Engineering, Center for Marine-Integrated Biotechnology (BK21 Plus), Pukyong National University, Busan 48513, Republic of Korea*

*[c]Interdisciplinary Program of Biomedical Mechanical & Electrical Engineering, Pukyong National University, Busan 48513, Republic of Korea*

*[d]Department of Otolaryngology – Head and Neck Surgery, Kosin University, College of Medicine, Busan 48513, Republic of Korea*

† Electronic supplementary information (ESI) available. See DOI: 10.1039/c7ra02140b

penetration, in tissues.[5] Therefore, multifunctional nanoparticles that could provide strong NIR absorbing capability are needed for the combined treatment of PTT and PDT. The multifunctional nanoparticles can be also used for image-guided combined therapy to target the treatment by taking advantage of using the same NIR laser photo-absorbers.

Polypyrrole (PPy) has been emerging as a super material for PTT because of its superior inherent features including strong NIR absorption, photothermal stability, low cost, and biocompatibility.[6,7] The photosensitizer-loaded on PPy has been recently developed to design the nano-platform for biomedical applications. For example, the photosensitizer chlorin e6 loading on PPy NPs which was used for a combination of PTT and PDT.[8] However, the chlorin e6 is not cost-effective and not soluble in water. Also, chlorin e6 is not approved by FDA for medicine. Moreover, their study used two different wavelength lasers to excite PDT and PTT separately which may cause difficulties in the treatment processing. Another research group used chlorin e4 as a photosensitizer loading on PPy NPs for PDT treatment.[9] Nonetheless, the costly synthesizing processing due to the expensive photosensitizer is a barrier for further applications of their system. Also, chlorin e4 is not approved by FDA for medicine.

Methylene blue (MB) is a common photosensitizer for PDT in clinical use with the cheap price.[10] MB is also a hydrophilic photosensitizer with a high quantum yield of singlet oxygen ($^1O_2$) generation.[10] Besides, MB is one of few PSs which were approved by FDA.[11,12] Generally, the ROS generated by MB induces cell death following apoptosis pathway that is less harmful to the patient than necrosis pathway. As most other PSs, however, the weak absorption on near-infrared (NIR) region of MB has narrowed the ability of light to penetrate into tissues.

To overcome the limitation of MB-based PDT, we introduced the facile and economic synthesis of MB encapsulated PPy nanoparticles to fabricate a novel NIR photo-absorber for a combination of PTT and PDT. We observed that the prepared polypyrrole–methylene blue nanoparticles (PPy–MB NPs) enable the remarkable generation of ROS by 808 nm laser irradiation that improves the deep tissue treatment of MB. The PPy–MB NPs also performed excellent photothermal behavior with the rapid increase of temperature under NIR laser irradiation. *In vitro* test confirmed the effectiveness of the PPy–MB NPs in killing the cancer cells with NIR laser irradiation. Furthermore, the phantom test of the photoacoustic microscopy (PAM) in conjunction with PPy–MB NPs showed a strong photoacoustic (PA) signal evenly with PPy–MB NPs at a quite low concentration (63 µg ml$^{-1}$), which shows the potential for PA imaging. Therefore, the PPy–MB NPs have the potential as single multifunctional nanoplatforms for NIR photo-induced therapy and photoacoustic imaging.

## 2. Materials and methods

### 2.1. Material

Pyrrole (Py, reagent grade, 98%), methylene blue (MB), polyvinyl alcohol (PVA, $M_w$: 9000–10 000), ferric chloride hexahydrate (FeCl$_3$·6H$_2$O), dimethyl sulfoxide (DMSO), sodium dodecyl sulfate (SDS), 1,3-diphenylisobenzofuran (DPBF), and 3-(4,5-dimethylthiazol-2-yl)-2,5-diphenyltetrazolium bromide (MTT) were purchased from Sigma-Aldrich (St. Louis, MO, USA), and were used as received during experiment. Breast cancer cells MDA-MB-231 and normal human dermal fibroblasts cells NHDF-Neo were purchased from Korean Cell Line Bank and Lonza, respectively. Cellular staining reagents including trypan blue, propidium iodide (PI) Hoechst 33342, acridine orange (AO), and dichlorodihydrofluorescein diacetate (DCFH-DA) were also purchased from Sigma-Aldrich (St. Louis, MO, USA). Dulbecco's modified Eagle's medium (DMEM), fetal bovine serum (FBS), penicillin, streptomycin, 1× trypsin, and phosphate buffered saline (PBS) were purchased from HyClone (South Logan, UT, USA). Distilled water (DW) was used for all experiments.

### 2.2. Synthesis of polypyrrole–methylene blue nanoparticles

The uniform polypyrrole nanoparticles (PPy NPs) were synthesized *via* one-step aqueous dispersion polymerization using PVA as a stabilizer, as reported elsewhere.[13] The use of PVA not only enhances the biocompatibility but also prolongs the immune response from PPy NPs.[14,15] SDS plays an important role in the loading of MB to PPy NPs. MB is a cationic photosensitizer which has a strong interaction with an anionic surfactant SDS *via* the electrostatic interaction. The anionic surfactant SDS interacted with the cationic backbone of PPy. Consequently, MB can interact with PPy *via* SDS link.

The overall synthesis procedure of PPy–MB NPs is schematically illustrated in Scheme 1a. Briefly, 10 mg of SDS and 1.50 g PVA were dissolved in 20 ml DW at 60 °C for 20 minutes. At first, the amount of MB was added to the above solution under the continuous stirring condition for 10 minutes. To investigate the
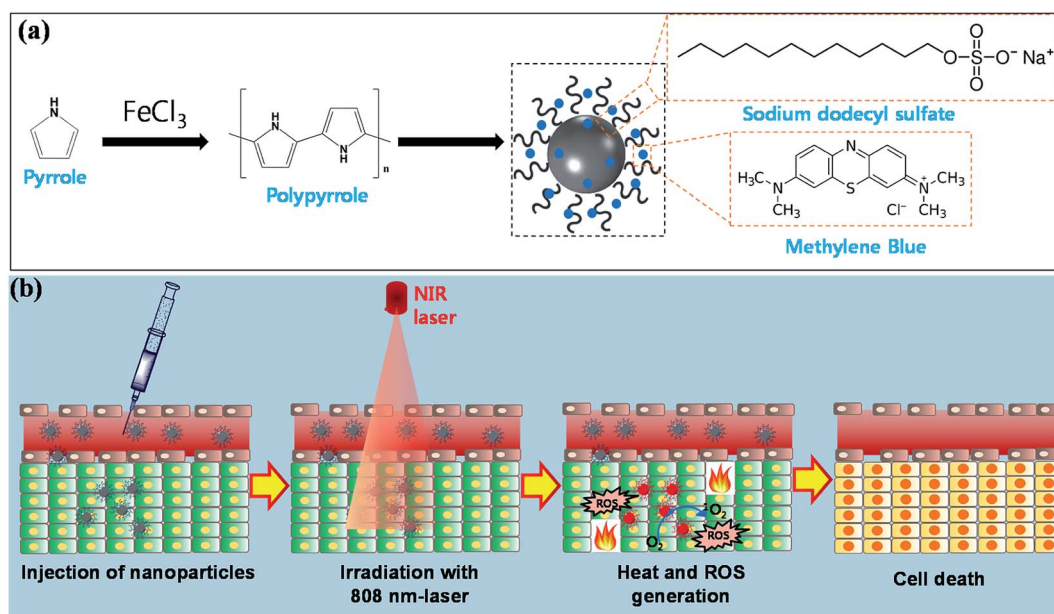


**Scheme 1** Schematic representation for (a) the synthesis and (b) the applications of PPy–MB NPs.

MB loading capacity, different amounts of MB (1, 1.5, 2, 2.5, and 3 mg) were used. Then the solution obtained was cooled to room temperature. Next, 0.67 g $FeCl_3 \cdot 6H_2O$ was added to the stirred PVA solution. After 1 hour of equilibration, pyrrole monomer (72 μL) was put into the above PVA/iron cation complex. The mixture turned black after a few minutes and the chemical oxidation polymerization of pyrrole was carried out for 4 hours. After that, the obtained nanoparticles were separated from the mixture by centrifugation (15 000 rpm, 40 minutes) and were washed several times with hot water to extrude impurities. All wash solution was collected to calculate the unload amount of MB by the UV-Vis absorption of the MB at 668 nm. The 668 nm-based standard curve of MB was provided in Fig. S1a (ESI†). The amount of loaded MB was computed by subtracting unloaded MB. The loading ratio of MB was calculated using the formula (mass of MB/mass of PPy–MB NPs) × 100%. The as-prepared PPy–MB NPs were re-suspended in DW at desired concentration.

In the synthesis processing, SDS was introduced as an emulsifier and it worked as a negative link between positive-photosensitizer and positive-polypyrrole core. We expected the increasing of the adding amount of SDS led to the increasing of the loading amount of MB onto the PPy NPs. Hence, we also examined 50 mg of SDS linker for the synthesis of PPy–MB NPs.

The release of MB was investigated by dialysis method. We kept the solution containing PPy–MB NPs on the dialysis bag (molecular weight cutoff is 7000 Da) and put on the baker containing the 200 ml PBS (pH 7.2 and pH 5.5). The above system was stirred for 48 hours. Then, the PBS buffer was collected and its UV-Vis absorption was recorded.

### 2.3. Characterization

The morphology of the synthesized particles was observed using a field emission scanning electron microscopy (FESEM; JSM-6700, JEOL, Japan). To analyze the functional groups of the prepared nanoparticles, a sample of the dried nanoparticles was mixed with KBr for the FTIR analysis over a wavelength range of 500–4000 $cm^{-1}$ at a resolution of 4 $cm^{-1}$ (Perkin-Elmer 1320 FTIR spectrophotometer). The particle size was determined by the dynamic light scattering (DLS) method using electrophoretic light scattering spectrophotometer (ELS-8000, OTSUKA Electronics Co. Ltd., Japan). The zeta potential was measured with an electrophoretic light scattering spectrophotometer (ELS-8000, OTSUKA Electronics Co. Ltd., Japan) using ELS FlatBoard cell. UV-Vis-NIR spectra were measured by using a UV-Vis-NIR spectroscopy (Thermo Biomate 5 Spectrophotometer). Laser irradiation was performed using an optical-fiber-coupled power-tunable diode laser (808 nm, continuous wave) (maximal power = 5 W, Hi-TechOptoelectronics Co., Beijing, China).

### 2.4. Singlet oxygen generation test: DPBF assay

DPBF assay[16,17] was used to measure the efficacy of singlet oxygen ($^1O_2$) generation of PPy–MB NPs under NIR laser irradiation. Briefly, 3 ml of 10 μg $ml^{-1}$ PPy–MB NPs was put in a cuvette with an optical path length 1 cm along with 10 μM of DPBF dissolved in DMSO. The cuvette was irradiated by an NIR laser at 0.5 W $cm^{-2}$ power density for every 5 minutes and the corresponding absorbance at 418 nm was recorded. A sample of PPy–MB NPs which had not been exposed to the laser irradiation was also prepared for comparison.

### 2.5. Photothermal test

For measuring the photothermal performance, a suspension (1 ml) containing the PPy–MB NPs with different concentrations (10, 20, 30, 50, 70, and 100 μg $ml^{-1}$) was put in a 12-well plate. Then each well was irradiated by NIR laser at a different power density of 0.5, 1, and 1.5 W $cm^{-2}$ for 6 minutes. The temperature was recorded by a thermometer (MASTECH, CA, USA) via a thermal fiber.

### 2.6. Long-term storage stability

The aqueous suspension PPy–MB NPs at 60 μg $ml^{-1}$ concentration was stored at 4 °C for 60 days to evaluate its stability in long-term storage. For the comparison, the UV-Vis absorption spectra and the particles size of PPy–MB NPs were observed for the 1st day and the last day. In addition, the zeta potential of stored PPy–MB NPs was monitored every 3 days during 12 days. The DPBF assay also was performed using the PPy–MB NPs of the last day for evaluating the stability of singlet oxygen generation of PPy–MB NPs. Besides, PPy–MB NPs on different media including distilled water, DMEM media, and PBS were stored at 4 °C for 20 days to evaluate the stability of prepared PPy–MB NPs.

### 2.7. Photostability tests

Three different ways were employed to evaluate the photostability of PPy–MB NPs. As the first way, the long-term irradiation under laser was conducted. The suspension PPy–MB NPs at 30 μg $ml^{-1}$ concentration was exposed to NIR laser at power density 0.5 W $cm^{-2}$ till the highest temperature was achieved and then it was allowed to return to the room temperature by turning the laser off. The heating and cooling cycles were repeated 6 times. As the second way, the PPy–MB NPs at the same concentration was exposed to NIR laser at power 0.5 W $cm^{-2}$ for 25 minutes. The UV-Vis absorption spectra of PPy–MB NPs were recorded for 5 minutes each. As the third way, the PPy–MB NPs in aqueous solution was irradiated with 808 nm laser at power density 1 W $cm^{-2}$ for 1 hour. Then, the samples were centrifuged and dried under vacuum before recording the FTIR.

### 2.8. *In vitro* cell cytotoxicity assay

The cell cytotoxicity assay on the model normal cell line and model cancer cell line to test the biocompatibility of PPy–MB NPs were performed. In this test, NHDF-Neo cells were used as a model normal cell line and MDA-MB-231 breast cancer cells were used as a model cancer cell line. The cells were cultured in DMEM medium containing 10% FBS and 1% antibiotics in a humidified atmosphere at 37 °C with 5% $CO_2$. A standard MTT assay[18] was used to quantify the cell cytotoxicity. The cells were seeded in 96-well plates at 1 × 10⁴ cells per well. After cell

attachment, the PPy–MB NPs suspended in growth medium at different concentrations (0, 50, 100, 200, 300, 400, 500, 600, 700, 800, 900, and 1000 $\mu g\ ml^{-1}$) were added to cell cultures and the treated cells were then incubated for 24, 48 and 72 hours. Next, 100 $\mu l$ MTT dissolved in PBS at 0.5 mg $ml^{-1}$ was added to each well and the microplates were further incubated for 4 hours at 37 °C with 5% $CO_2$. Dissolved MTT was converted to insoluble purple formazan product by cleavage of the tetrazolium ring via dehydrogenase enzyme that is present in the mitochondria of the active cells. The insoluble purple formazan was dissolved in 100 $\mu l$ DMSO and its absorbance was recorded at 570 nm using a plate reading spectrophotometer to quantify the percentage of cell viability.

In addition, the fluorescent images of MDA-MB-231 breast cancer cells with AO and PI staining also were captured to analysis the biocompatibility of the prepared PPy–MB NPs.

## 2.9. In vitro combined photothermal and photodynamic therapy

The MTT assay was performed to compare the efficacy of PPy NPs and PPy–MB NPs on killing capability of MDA-MB-231 breast cancer cells. Briefly, the MDA-MB-231 cells were seeded in a 96-well plate at a density of $1 \times 10^4$ cells per well. Then, the cells were treated with the PPy NPs and PPy–MB NPs for 24 hours and unbound nanoparticles were washed with PBS. After that, the cells were exposed to NIR laser at a power density of 0.5 W $cm^{-2}$ for 6 minutes. To obtain the results, the following steps were conducted in accordance with the in vitro cell cytotoxicity assay in Section 2.8.

In addition, the damaged and the dead cells were determined using the double staining of Hoechst 33342 and PI to evaluate the efficacy of combined photothermal and photodynamic treatment. Concretely, the MDA-MB-231 cells were seeded in a 12-well plate at a density of $1 \times 10^5$ cells per well. Then, the cells were treated with the PPy NPs (50 $\mu g\ ml^{-1}$) and PPy–MB NPs (50 $\mu g\ ml^{-1}$) for 24 hours and unbound nanoparticles were washed with PBS. After that, the cells were exposed to NIR laser at a power density of 0.5 W $cm^{-2}$ for 6 minutes. Cells with and without nanoparticles which had not been exposed to the laser irradiation were also prepared for the comparison. Next, the cell plates were kept for further 4 hours in the incubator and then the treated and untreated cells were stained with Hoechst 33342 and PI. The cell culture plate was added 1.5 ml Hoechst 33342 (10 $\mu g\ ml^{-1}$) and then kept in the incubator for 20 minutes. After that, the cells were washed with PBS to remove the excess stain. Following this, the cells were continuously stained with 1.5 ml PI (10 $\mu g\ ml^{-1}$) and incubated at room temperature for 5 minutes. Finally, the cells were carefully washed with PBS and the fluorescent images were taken by a fluorescence microscope (Leica Microsystems GmbH, Wetzlar, Germany).

## 2.10. Intracellular ROS detection: DCFH-DA staining

To detect the generated ROS, dichlorodihydrofluorescein diacetate (DCFH-DA), which is the most commonly used probe,[19] was employed. First, MBA-MD-231 cells ($1 \times 10^5$) were seeded in a 12-well plate and treated with the PPy–MB NPs (50 $\mu g\ ml^{-1}$). After 24 hours incubation, the treated cells were washed with PBS to remove unbound nanoparticles, then each well was illuminated with an NIR laser at a power density of 0.5 W $cm^{-2}$ for 6 minutes. Irradiated cells were incubated for 1 hour. Next, 10 mM DCFH-DA was added to the cell culture plate and the cells were incubated for further 30 minutes. Finally, the stained cells were washed with PBS (3 times) and the fluorescent images were captured using the fluorescence microscope. Samples of the irradiated cells with PPy–MB NPs and non-irradiated cells without nanoparticles were also prepared for the comparison.

## 2.11. In vitro photoacoustic imaging

Based on the previous study,[20] we built the PAM high power laser diode with some modifications. Fig. S10 (ESI†) shows the optical resolution of PAM system which was configured with a transmission mode where the laser is opposite to the transducer. A high power pulsed laser diode (LD, Laser Components, 905D5S2L3J08U) was employed as an excitation source. It uses the stacked arrays with five active elements, which provides the emitting area of 800 × 440 $\mu m^2$. A driver (PicoLAS, LDP-V 240-100 V3) helps the pulsed laser diode operate normally at a 905 ± 15 nm, which produces a peak power output up to 650 W. The PRF trigger 800 Hz, with duty factor 0.1%, allows the LD to work with a pulse duration of 150 ns. A group of lens consisting of the collimation tube (Thorlabs, LTN330-C) and focusing lens (S. Plan 40×, NA = 0.1) was used to collimate and focus the beam onto the phantom. A function generator (HP, 33120A) triggered the driver and the data acquisition (NI-DAQ) board at the same time through TTL (Transistor–Transistor-Logic) trigger. The photoacoustic signal was collected by the commercially focused transducer (Olympus Panametrics, NDT-V308) with a center frequency of 5 MHz. Firstly, the signal was magnified by a preamplifier (26 dB) (Mini-Circuits, ZFL – 500LN). Next, it was amplified once again by pulser/receiver with an amplified gain of 54 dB at low noise input at 1 kHz to 20 MHz bandwidths. Finally, these signals were acquired by DAQ PC to reconstruct the 2D images by PXI-5122 (National Instruments, USA) features with a 12 bit analogue-to-digital converter with a maximal sampling rate of 100 MHz. The scanning was performed by two DC motors (Newport Motor) that move the phantom in $X$ and $Y$ directions as a raster scan. In the transmission mode, the distance between the optical lens, the ultrasound transducer and the sample was adjusted to achieve the maximum amplitude signal. The total system operation and data procession were performed on Labview Full Development System (Version 14, NI, USA).

To get the in vitro photoacoustic imaging, different concentrations of PPy–MB NPs were applied in a phantom which was made of silicon tubes ($N = 5$). Various concentrations of PPy–MB NPs were filled in the tubes (Fig. 8a) and tested (i.e., 63 $\mu g\ ml^{-1}$, 125 $\mu g\ ml^{-1}$, 250 $\mu g\ ml^{-1}$, and 500 $\mu g\ ml^{-1}$). The phantoms were placed in a water tank for PAM. For the comparison, the same concentrations of PPy NPs were also prepared in the same way.

# 3. Results and discussion

## 3.1. Synthesis and characterization of polypyrrole–methylene blue nanoparticles

The synthesis of uniform PPy–MB NPs is illustrated in Scheme 1a. The monodisperse PPy–MB NPs were prepared *via* chemical oxidation polymerization using $Fe^{3+}$ as the oxidizing agent and PVA as the stabilizer. The surface charge at each stage of the synthesizing process is shown in Fig. S3a (ESI†). The zeta potential of pure PPy NPs was +14.77 mV, which was caused by the positive backbone of PPy. After SDS adding, the zeta potential of the system changed to −37.71 mV. This indicated that the adsorption of negatively charged SDS molecules assigned the nanoparticles an overall negative charge. It is observed that the loading of MB, cationic dye, led to the change of surface charge to −28.47 mV. As expected, the less negative zeta potential presented when a positively charged compound was loaded. The average diameter of nanoparticles increased about 2 nm after adding SDS molecules (Fig. S3a, ESI†). It is found that the particle size remained nearly-unchanged before and after loading MB.

The UV-Vis-NIR absorption spectra of MB, PPy, and PPy–MB NPs are given in Fig. 1a. It is observed that MB had a strong absorption peak at 668 nm and the presence of this peak in the PPy–MB NPs confirmed the success of loading of MB onto PPy NPs. The formation of the matrix PPy–SDS–MB formed novel nanoparticles which enable high near-infrared absorbing properties (Fig. 1a). We found that the loading capacity of MB on PPy NPs was saturated at 2.4% with 2.5 mg feeding amount of MB (Fig. S1b, ESI†). To increase the loading amount of MB onto the PPy NPs, 50 mg of SDS linker was used as a description in Section 2.2. As expected, the PPy–MB with the higher feeding amount of SDS exhibited higher absorption amplitude which indicated the higher loading amount of MB (Fig. 1b). However, when feeding amount of SDS was 50 mg, the PPy–MB particles with micrometer diameter (∼2 μm) were formed (Fig. 2c and d). Meanwhile, with 10 mg feeding amount of SDS, the nanoparticles exhibited the uniform spherical morphology within 30 and 70 nm. The size of nanoparticles should be designed between 10 and 50 nm in diameter to increase bloodstream circulation time.[21] Furthermore, the micrometer-size particles

can lead to capillary blockade and embolism that could cause serious damages to patients. Thus, the PPy–MB NPs with an average of 48.5 nm (Fig. 2a) will be used in all the following experiments.

The stable binding of MB on PPy NPs is really important for the PDT at NIR range. The de-attached MB can be detected by dialysis method. The collected PBS buffer (pH 7.2 and pH 5.5) after 48 hours stirring did not emit any absorbance peak for MB, indicating the stable binding of MB on PPy NPs. This experimental observation was consistent with the previous report, which suggested that the cation drug, rhodamine 6G, cannot be released out of PPy NPs on a range of biological pH tested.[22]

The optical properties of PPy–MB in aqueous dispersions with different concentrations (10 to 100 μg ml$^{-1}$) were studied by the UV-Vis-NIR spectroscopy. As plotted in Fig. 3a, with the increase of PPy–MB NPs concentration, the photoabsorption intensity went up in the entire UV-Vis-NIR region and all spectra exhibited the absorption peak of MB at approximately 668 nm. The standard curve of PPy–MB NPs following the 808 nm absorption point (Fig. S2, ESI†) has validated that the absorption amplitude increased linearly with the PPy–MB concentration ($R^2 = 1$).

FTIR was also implemented to confirm the loading of MB onto the PPy NPs by examining the FTIR frequency changes. Fig. 3b shows the FTIR spectra of the synthesized PPy and PPy–MB NPs. Overall, the prominent peaks were observed for both PPy and PPy–MB NPs spectra. Specifically, the FTIR vibration bands at 1554 cm$^{-1}$ and 1465 cm$^{-1}$ were assigned to N–H stretching vibrations of PPy ring. The band at 1173 cm$^{-1}$ was attributed to C–N stretching vibration and the band at 783 cm$^{-1}$ indicated that the presence of polymerized pyrrole.[23] The FTIR vibration bands at 2855 and 2919 cm$^{-1}$ were corresponding to C–H stretching, and the C–H stretching vibration the intensity of this group was increased in the case of PPy–MB NPs due to the presence of SDS and the methyl group of MB. The broad peak at 1318 cm$^{-1}$ for the sample PPy–MB NPs indicated that the MB molecules interacted with SDS groups through electrostatic interactions. The FTIR spectra confirmed the formation of PPy NPs and the presence of loaded MB molecules onto the PPy NPs.
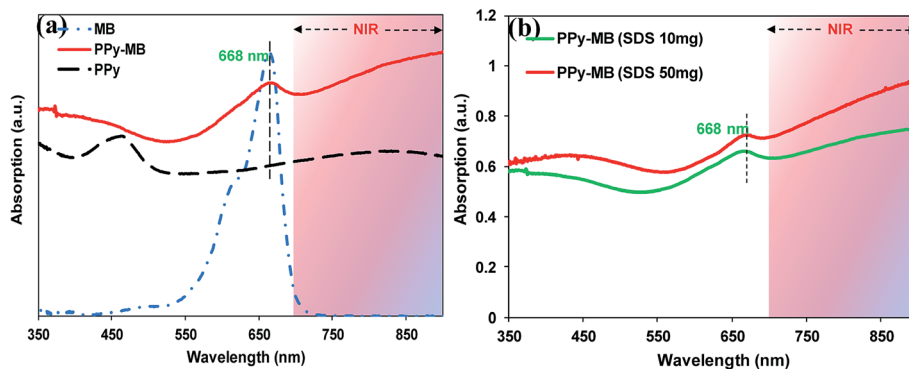


Fig. 1 (a) The UV-Vis absorption methylene blue, PPy, and PPy–MB NPs. (b) The UV-Vis absorption of 100 μg ml$^{-1}$ PPy–MB NPs two conditions (SDS 10 mg and SDS 50 mg).
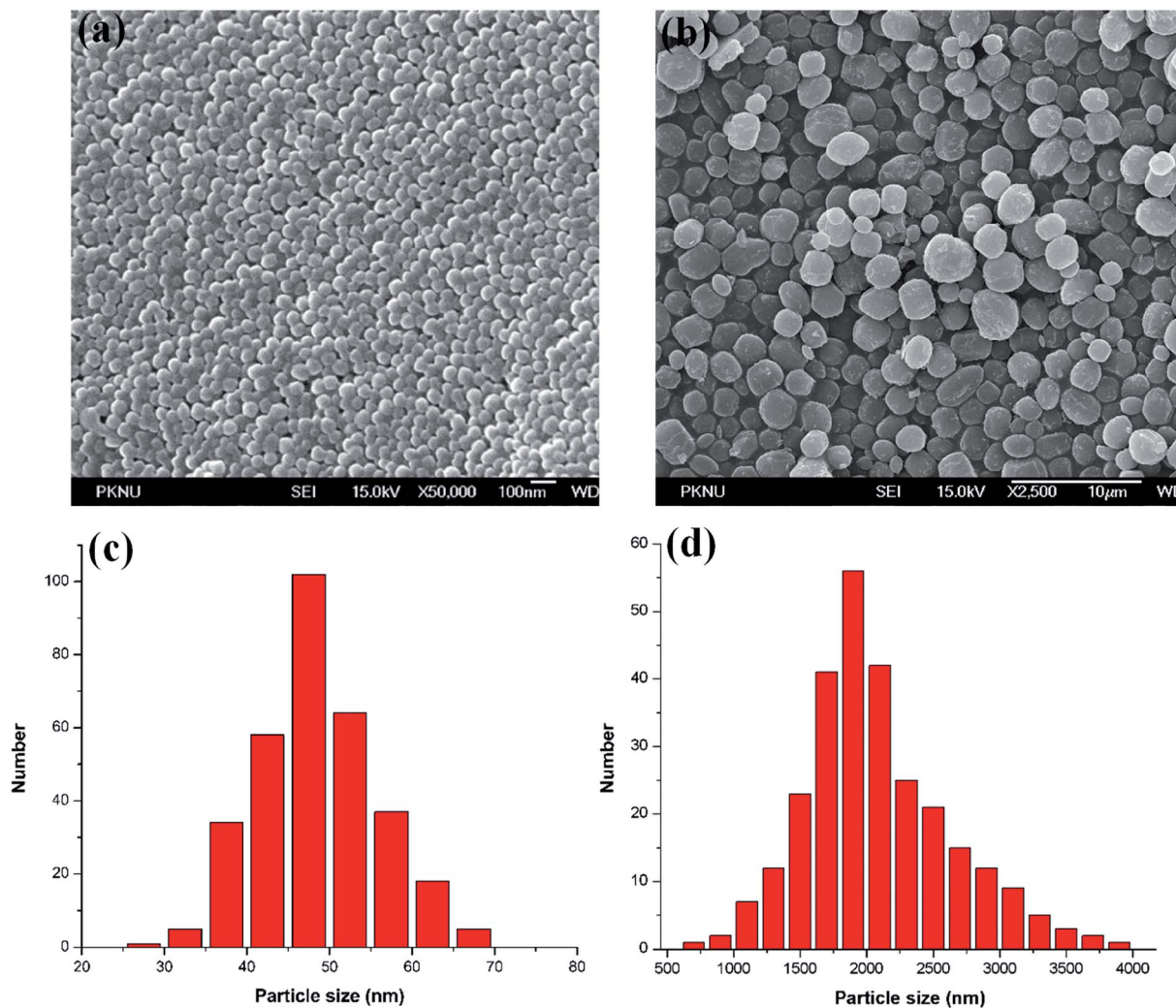
Fig. 2    The SEM of PPy–MB NPs with (a) SDS 10 mg and (b) SDS 50 mg. (c) and (d) Corresponding size distributions of PPy–MB NPs.
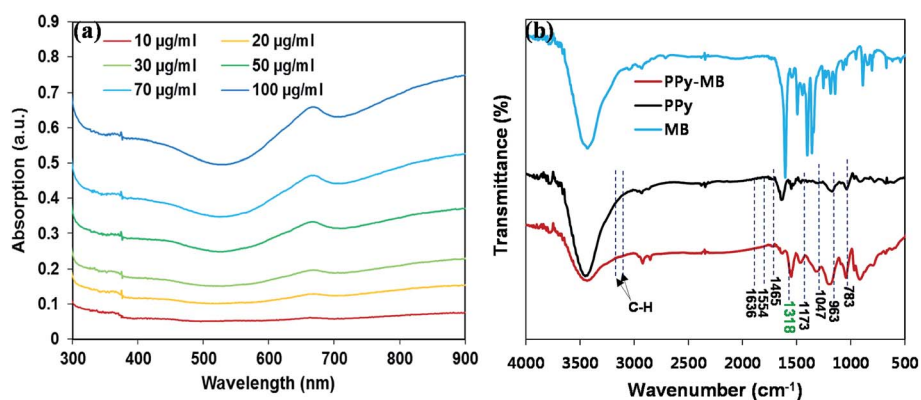


Fig. 3    (a) The UV-Vis-NIR spectra of PPy–MB NPs with different concentrations. (b) FTIR of MB, PPy and PPy–MB NPs.

### 3.2.    Photothermal performance of polypyrrole–methylene blue nanoparticles

We evaluated the photothermal effect of PPy–MB NPs at different concentrations under NIR laser at 0.5, 1, and 1.5 W cm$^{-2}$ for 6 minutes. As shown in Fig. 4a–c, the temperature of the solution containing PPy–MB NPs increased with the increment of the exposure time and the concentration of PPy–MB NPs. Under the same NIR laser condition (6 minutes at 0.5 W

cm$^{-2}$), the temperature of the solution containing 10 µg ml$^{-1}$ PPy–MB NPs increased to 38 °C while that containing 50 µg ml$^{-1}$ PPy–MB NPs reached up to 50 °C. It is also observed that when the NIR laser power density was increased, the temperature of the photothermal material also went up. As the laser power density increased up to 1.5 W cm$^{-2}$, the temperature of the solution containing 50 µg ml$^{-1}$ PPy–MB NPs rapidly reached 50 °C within a short time (2 minutes). These experimental results revealed that the exposure time, the concentration of nanoparticles and the laser power intensity are important parameters that significantly influenced the photothermal performance of PPy–MB NPs.

### 3.3. Photodynamic property of polypyrrole–methylene blue nanoparticles

Polypyrrole is the conducting polymers (also called synthetic metals) which owns electronic properties of metals while keeping the mechanical characterizations of conventional polymers.[24] In other words, polypyrrole has high free-electron mass as metal. Thus, PPy–MB NPs could generate $^1O_2$ under 808 nm irradiation because PPy–MB NPs has a strong absorption at NIR region (Fig. 1a) which facilitates the electron transfer from the PPy to the MB molecules.

DPBF interacts with $^1O_2$ and converts to o-dibenzoylbenzene (DBB).[25] The amount of DPBF consumption can be monitored by measuring the absorbance at 418 nm. In other words, the decrease of the UV-Vis absorption of DPBF at 418 nm indicated the $^1O_2$ generation of the sample. When the DPBF and PPy–MB NPs mixture exposed to an NIR laser during 25 minutes, the dramatic decrease of the absorbance at 418 nm was observed, as shown in Fig. 5a and b. The fast decreased absorbance

confirmed the remarkable generation of $^1O_2$ of nanoparticles after irradiation. In contrast, no consumption of DPBF was observed in the sample containing only DPBF. The non-irradiated DPBF along with PPy–MB NPs sample also showed negligible DPBF consumption.

### 3.4. Long-term storage stability tests of polypyrrole–methylene blue nanoparticles

To evaluate the stability, the zeta potential, the size, and the UV-Vis-NIR absorption of the prepared nanoparticles were monitored over the storage. Fig. S3 (ESI†) shows the zeta potential of the PPy–MB NPs recorded within 12 days of storage. According to the figure, the surface charge of the nanoparticles was found nearly-constant during the storage. The particle size after 60 days in storage was measured, as shown in Fig. S4d (ESI†). After 60 days, the average particle size was found as around 49.5 nm, which was almost the same as the one of the first day. So far, the PPy–MB NPs in DW at 60 µg ml$^{-1}$ concentration did not show any change in its UV-Vis-NIR spectra (Fig. S4a, ESI†) after two months of storage. Furthermore, the ability in the singlet oxygen generation of PPy–MB NPs of the last day (after 60 days) was similar with that of the first day, as reported in Fig. S4b (ESI†). And, no aggregation was observed in all solution containing PPy–MB NPs (Fig. S4c, ESI†). All the above results proved the inherent stability of the prepared nanoparticles.

### 3.5. Photostability tests of polypyrrole–methylene blue nanoparticles

After six cycles of heating and cooling under an NIR laser irradiation at the power density of 0.5 W cm$^{-2}$, the thermal curve of
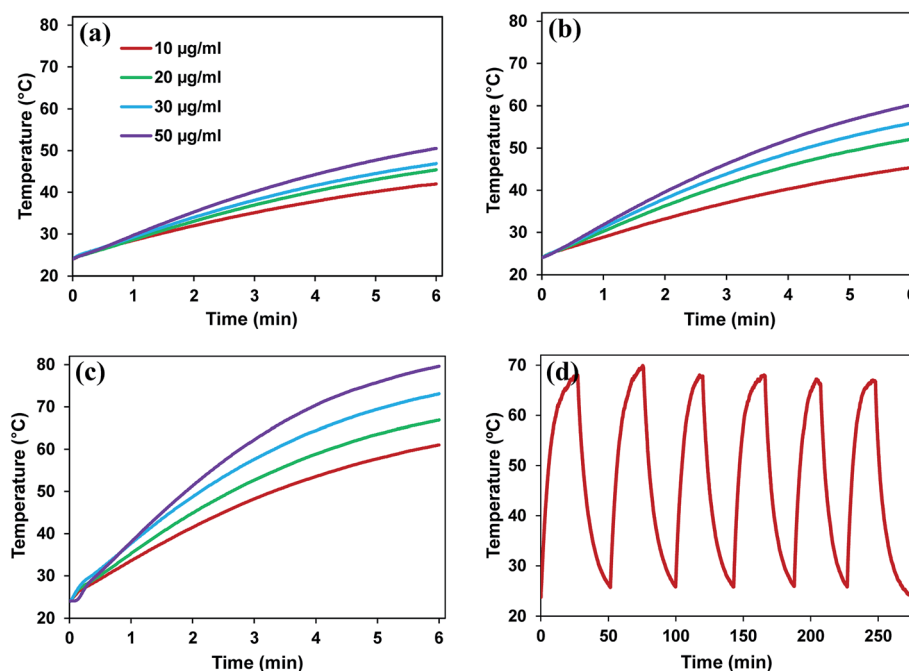


Fig. 4 The photothermal decay of PPy–MB NPs with different concentrations and different power densities. All solutions were irradiated with (a) 0.5 W cm$^{-2}$, (b) 1 W cm$^{-2}$, and (c) 1.5 W cm$^{-2}$ 808 nm laser for 6 minutes. (d) The real-time temperature record of 6 heating/cooling cycles of 30 µg ml$^{-1}$ PPy–MB NPs under on/off laser experiment (1 W cm$^{-2}$).
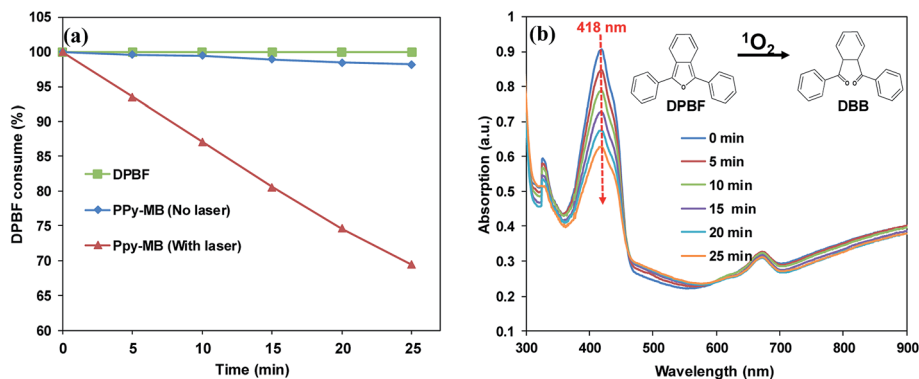
Fig. 5 (a) Decay profiles of the DPBF consumed in the absence of PPy–MB NPs (green) and in the presence of PPy–MB NPs (at 50 μg ml$^{-1}$ concentration) without laser (blue) and with 808 nm laser at 0.5 W cm$^{-2}$ (red). (b) The production of singlet oxygen by PPy–MB NPs (at 50 μg ml$^{-1}$ concentration) with 808 nm laser at 0.5 W cm$^{-2}$ and the reaction mechanism of $^1O_2$ with DPBF were inserted at the top-right corner of the graph.

PPy–MB NPs remained almost the same for each cycle, indicating good photothermal stability of PPy–MB NPs (Fig. 4d). This property is important for the PTT treatment.

To the PDT treatment, the amount of ROS induced by irradiated nanoparticles is an essential parameter. To obtain the stable amount of ROS, the PPy–MB NPs should resist the photobleaching of the MB under the light. NIR laser excitation of PPy–MB NPs during 25 minutes showed a stable absorption band (Fig. S5, ESI†). This result indicated that the PPy–MB NPs remained the ability to generate the stable amount ROS.

The FTIR before and after laser exposure was shown in Fig. S6 (ESI†). As shown in the figure, the peak positions and intensities of the irradiated sample are well-consistent to those of the non-irradiated sample. This result revealed that the chemical structure of PPy–MB NPs was stable even after 1 hour of irradiation.

### 3.6. *In vitro* cell cytotoxicity assay

As shown in Fig. S7 (ESI†), PPy–MB NPs have a low cytotoxicity to MDA-MB-231 breast cancer cells and also low cytotoxicity to NHDF-Neo normal cells. No significant cytotoxicity of PPy–MB NPs was observed even at a highest tested concentration (1000 μg ml$^{-1}$), where the cell viability of NHDF-Neo cells was still higher than 85%. Under 100 μg ml$^{-1}$, PPy–MB NPs have really low cytotoxicity to both normal and cancer cells. In addition, the fluorescent images of MDA-MB-231 cells incubated with PPy–MB NPs for 24 hours were shown in Fig. S8 (ESI†). The green indicated the live cells and the red indicated the dead cells. The number of dead cells is trivial. The above observations indicated that PPy–MB NPs are biocompatible nanoparticles.

### 3.7. *In vitro* combined photothermal and photodynamic therapy

The MTT assay was performed to compare the efficacy of irradiated PPy and PPy–MB NPs on killing capability of MDA-MB-231 breast cancer cells. As shown in Fig. S9 (ESI†), the percentage of cell viability was gradually decreased when the concentration of treated nanoparticles was increased. More than 60% of cell died at a 50 mg ml$^{-1}$ concentration of

irradiated PPy–MB NPs; meanwhile, only about 30% of cell death was observed for the same concentration of the irradiated PPy NPs. This result indicated that the irradiated PPy–MB NPs can kill much more cells than the irradiated PPy NPs at the same concentration.

In addition, we compared the killing capability of cancer cells by the fluorescence imaging techniques of five groups: the control groups (only cells), the laser only group (cells were treated with 808 nm laser), the PPy NPs group + 808 nm laser (cells were treated with PPy NPs + 808 nm laser), the PPy–MB NPs group (cells were treated with PPy–MB NPs), and the PPy–MB NPs + 808 nm laser group (cells were treated with PPy–MB NPs + 808 nm laser). Based on the heating curve and the ROS generation graph of PPy–MB NPs, we selected 50 μg ml$^{-1}$ concentration, the power density of 0.5 W cm$^{-2}$, and 6 minutes irradiation to set up the experiment. As shown in Fig. 4a and 5a, after exposing for 6 minutes at 0.5 W cm$^{-2}$, the sample containing 50 μg ml$^{-1}$ PPy–MB NPs reached up to 50 °C and the DPBF consumption was around 10%. As shown in Fig. S9 (ESI†), higher than 60% of cell death at a 50 mg ml$^{-1}$ concentration of irradiated PPy–MB NPs was observation. Furthermore, non-irradiated PPy–MB NPs at a 50 μg ml$^{-1}$ concentration showed a high biocompatible property with nearly 100% viable cells after 24 hours incubation (Fig. S7, ESI†).

Double staining of Hoechst 33342 and PI was used to explore the damaged and dead cells. Hoechst 33342 dye specific to DNA staining, which can be permeable in both dead and viable cells.[26] The changes in the size and shape of nuclei of the Hoechst 33342 stained cells can be observed under a fluorescence microscopy. PI dye also binds to DNA, but it only permeates through the membrane of damaged and dead cells.[27] So, double staining can reveal the damaged and dead cells by each treatment method. As shown in Fig. 6, only a few dead cells with the red nuclei were observed in the control, laser only, and the PPy–MB NPs group. In contrast, almost cells in the PPy–MB NPs + 808 nm laser group died with the red nuclei, as observed in Fig. 6e. For the PPy NPs + 808 nm laser group, not many dead cells were seen in Fig. 6c, even at the same concentration (50 μg ml$^{-1}$) and laser treatment (at 0.5 W cm$^{-2}$ for 6 minutes) with the
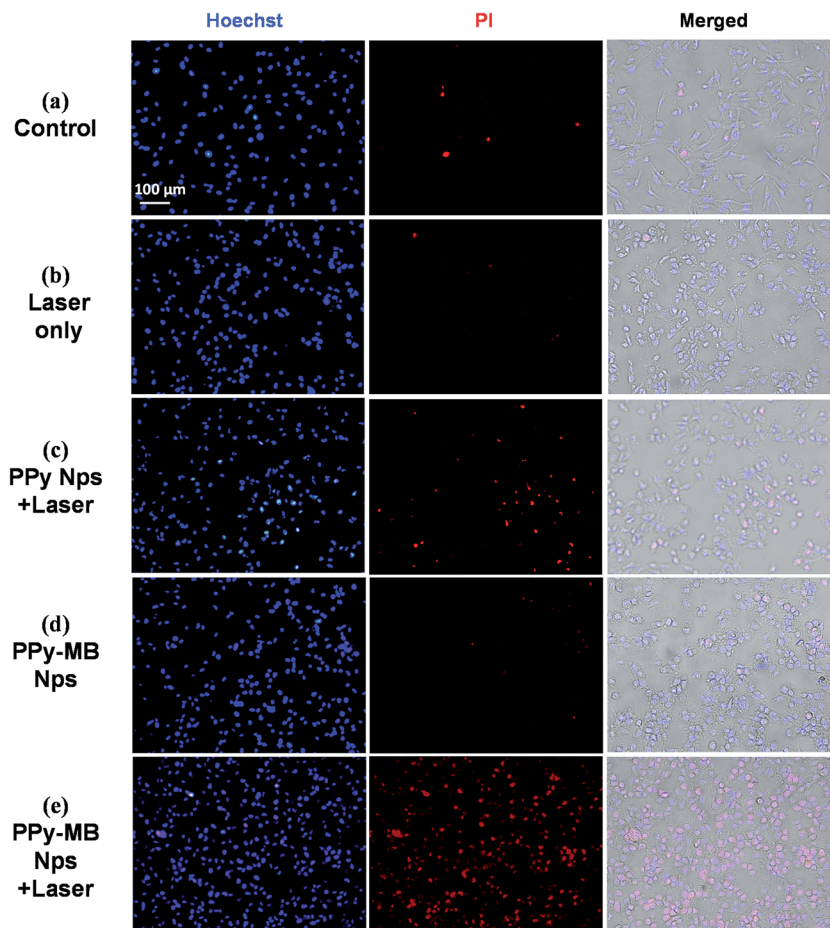
**Fig. 6** Fluorescence images of MDA-MB-231 cells under different conditions. (a) Control, (b) laser only (808 nm laser), (c) PPy NPs + 808 nm laser, (d) PPy–MB NPs, and (e) PPy–MB NPs + 808 nm laser. The concentration of PPy–MB NPs and PPy NPs were 50 $\mu g$ $ml^{-1}$ and the 808 nm laser (0.5 W $cm^{-2}$) irradiation was carried out for 6 minutes.

PPy–MB NPs + 808 nm laser group. Without 808 nm irradiation, PPy–MB NPs were not able to kill the cancer cell, as observed in Fig. 6d.

The cancer cell death by PPy–MB NPs group could be due to two main factors, including ROS, owing to MB; and heating, owing to PPy. The data clearly indicated that the PPy–MB NPs can be used for NIR-induced combined therapy and much more effective than a single therapy.

### 3.8. Intracellular ROS detection

Dichlorodihydrofluorescein diacetate (DCFH-DA) is the most common probe to detect intracellular ROS.[19] Due to its excellent permeability through cell membranes, DCFH-DA easily enters the cells and it is deacetylated to form DCFH carboxylate anion. When the ROS is presented in the cells, DCFH reacts with it and forms 2′,7′-dichlorofluorescein (DCF) which is fluorescent green.[28] After irradiating the cells with the NIR laser, the fluorescent images of DCF were taken, as shown in Fig. 7a–d. There were weak fluorescence images of DCF in the control group, laser only group, and PPy–MB NPs group. On the other hand, the strong fluorescent images were observed in PPy–MB NPs + 808 nm laser group. To quantify the DCF signals in the cells, the

intensity of green fluorescent DCF was analyzed using ImageJ program. As plotted in Fig. 7e, the PPy–MB NPs induced the highest ROS level among all the groups, indicating the promising effectiveness of PPy–MB NPs for the PDT.

### 3.9. *In vitro* photoacoustic imaging

PA imaging is an emerging imaging modality and can be used to assist phototherapy.[29] The PA imaging of the phantom with PPy–MB NPs is shown in Fig. 8b. All the samples containing nanoparticles were clearly visible, whereas the controlled tube with DW did not produce any PA signal. The image contrast was increased when the concentration of nanoparticles went up. The measured PA amplitudes increased linearly with the PPy–MB NPs concentrations with simple linear regression $R^2 = 0.91$ (Fig. S12, ESI†). For the comparison, the PA signal of phantom study with PPy NPs alone also was acquired. As shown in Fig. S10b (ESI†), PPy–MB NPs produced stronger PA signals than the PPy NPs. This phenomenon was caused by the UV-Vis absorption of PPy–MB NPs at 905 nm which was stronger than that of PPy NPs at the same concentration (Fig. S11a, ESI†).

The ability to image PPy–MB NPs inside phantom with the PAM system is very promising for image-guided photo-induced
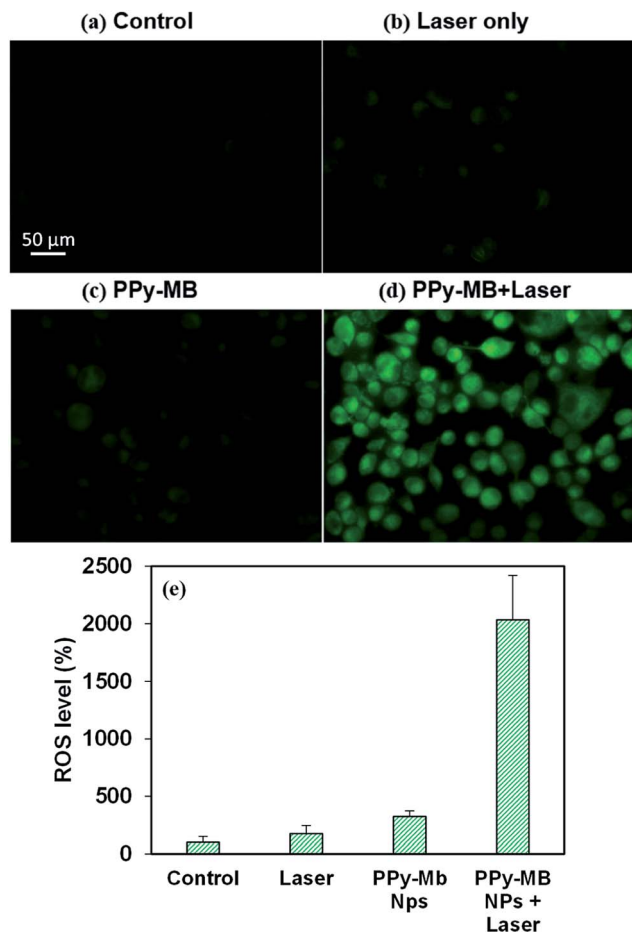
Fig. 7 Fluorescence images of DCF in MDA-MB-231 cells under different conditions. (a) Control, (b) laser only (808 nm laser), (c) PPy–MB NPs and (d) PPy–MB NPs + 808 nm laser. The concentration of PPy–MB NPs was 50 μg ml$^{-1}$ and the 808 nm laser (0.5 W cm$^{-2}$) irradiation was carried out for 6 minutes. (e) ROS level (fluorescence intensity per area) in each group (data are presented as a mean ± standard deviation).

cancer therapy. The laser system (905 nm) for PAM which was used in conjunction with PPy–MB NPs, also show a potential for the future implementation.
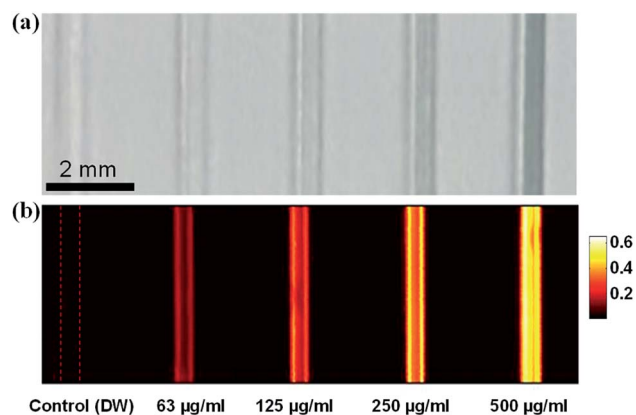


Fig. 8 Evaluations on PA responses of PPy–MB at various concentrations: (a) phantom (b) corresponding PA images.

## 4. Conclusion

In this study, we have newly developed multifunctional nanoparticles with broad NIR absorbing property that can be used to overcome the limitation of traditional PDT. The proposed system PPy–MB NPs showed the great potential for the deep tissue treatment using the combined photo-induced cancer therapy with a single near-infrared wavelength. The PPy–MB NPs not only generated heat effectively but also produced the remarkable amount of ROS under NIR laser irradiation. *In vitro* tests proved that combined PTT and PDT treatment was more effective than an individual treatment. Moreover, the strong PA signal of PPy–MB NPs was found to be promising for guiding photo-induced therapy. The proposed system is also cost-effective, biocompatible, and stable. In the future, *in vivo* studies will be conducted to evaluate the performance of the proposed system for photoacoustic image-guided combined photo-induced cancer therapy.

## Acknowledgements

## References

1 Z. Cheng, A. A. Zaki, J. Z. Hui, V. R. Muzykantov and A. Tsourkas, *Science*, 2012, **338**, 903–910.
2 S. S. Chandratre and A. K. Dash, *AAPS PharmSciTech*, 2015, **16**, 98–107.
3 H. Wang, Y.-L. Zhao and G.-J. Nie, *Front. Mater. Sci.*, 2013, **7**, 118–128.
4 J. Oh, H. Yoon and J.-H. Park, *Biomed. Eng. Lett.*, 2013, **3**, 67–73.
5 A. M. Smith, M. C. Mancini and S. Nie, *Nat. Nanotechnol.*, 2009, **4**, 710–711.
6 M. Chen, X. Fang, S. Tang and N. Zheng, *Chem. Commun.*, 2012, **48**, 8934–8936.
7 Z. Zha, Z. Deng, Y. Li, C. Li, J. Wang, S. Wang, E. Qu and Z. Dai, *Nanoscale*, 2013, **5**, 4462–4467.
8 X. Song, C. Liang, H. Gong, Q. Chen, C. Wang and Z. Liu, *Small*, 2015, **11**, 3932–3941.
9 D. Park, K. O. Ahn, K. C. Jeong and Y. Choi, *Nanotechnology*, 2016, **27**, 185102.
10 J. Yu, C. H. Hsu, C. C. Huang and P. Y. Chang, *ACS Appl. Mater. Interfaces*, 2015, **7**, 432–441.
11 T. Mito, T. Suzuki, T. Kobayashi, X. Zheng, Y. Hayashi, A. Shiraishi and Y. Ohashi, *Invest. Ophthalmol. Visual Sci.*, 2012, **53**, 6305–6313.
12 E. J. Lim, C. H. Oak, J. Heo and Y. H. Kim, *Oncol. Rep.*, 2013, **30**, 856–862.
13 J. Y. Hong, H. Yoon and J. Jang, *Small*, 2010, **6**, 679–686.
14 S. Omata, Y. Sawae and T. Murakami, *Biosurface and Biotribology*, 2015, **1**, 71–79.

15 T. S. Gaaz, A. B. Sulong, M. N. Akhtar, A. A. Kadhum, A. B. Mohamad and A. A. Al-Amiery, *Molecules*, 2015, **20**, 22833–22847.

16 K. Liu, X. Liu, Q. Zeng, Y. Zhang, L. Tu, T. Liu, X. Kong, Y. Wang, F. Cao, S. A. Lambrechts, M. C. Aalders and H. Zhang, *ACS Nano*, 2012, **6**, 4054–4062.

17 F. Ai, Q. Ju, X. Zhang, X. Chen, F. Wang and G. Zhu, *Sci. Rep.*, 2015, **5**, 10785.

18 T. Mosmann, *J. Immunol. Methods*, 1983, **65**, 55–63.

19 B. Kalyanaraman, V. Darley-Usmar, K. J. A. Davies, P. A. Dennery, H. J. Forman, M. B. Grisham, G. E. Mann, K. Moore, L. J. Roberts Ii and H. Ischiropoulos, *Free Radicals Biol. Med.*, 2012, **52**, 1–6.

20 T. J. Allen and P. C. Beard, *Opt. Lett.*, 2006, **31**, 3462–3464.

21 Z. Bao, X. Liu, Y. Liu, H. Liu and K. Zhao, *Asian J. Pharm. Sci.*, 2016, **11**, 349–364.

22 D. Samanta, J. L. Meiser and R. N. Zare, *Nanoscale*, 2015, **7**, 9497–9504.

23 S. Bose, N. H. Kim, T. Kuila, K. T. Lau and J. H. Lee, *Nanotechnology*, 2011, **22**, 295202.

24 V. V. Tat'yana and N. E. Oleg, *Russ. Chem. Rev.*, 1997, **66**, 443.

25 E. A. Mayeda and A. J. Bard, *J. Am. Chem. Soc.*, 1974, **96**, 4023–4024.

26 S. A. Latt and G. Stetten, *J. Histochem. Cytochem.*, 1976, **24**, 24–33.

27 L. C. Crowley, A. P. Scott, B. J. Marfell, J. A. Boughaba, G. Chojnowski and N. J. Waterhouse, *Cold Spring Harb. Protoc.*, 2016, **2016**, 087163.

28 J. F. Curtin, M. Donovan and T. G. Cotter, *J. Immunol. Methods*, 2002, **265**, 49–72.

29 J. L. Su, B. Wang, K. E. Wilson, C. L. Bayer, Y.-S. Chen, S. Kim, K. A. Homan and S. Y. Emelianov, *Expert Opin. Med. Diagn.*, 2010, **4**, 497–510.